

Complex-amplitude Fourier single-pixel imaging via coherent structured illumination

Ya-Nan Zhao,¹ Hong-Yun Hou,¹ Jia-Cheng Han,¹ De-Zhong Cao,²

Su-Heng Zhang,^{1,*} Hong-Chao Liu,^{3,†} and Bao-Lai Liang^{1,‡}

¹*Hebei Key Laboratory of Optic-Electronic Information and Materials,
College of Physics Science & Technology, Hebei University, Baoding 071002, China*

²*Department of Physics, Yantai University, Yantai 264005, China*

³*Institute of Applied Physics and Materials Engineering,
University of Macau, Avenida da Universidade, Taipa, Macao SAR, China*

(Dated: February 8, 2022)

We propose a method of complex-amplitude Fourier single-pixel imaging (CFSI) with coherent structured illumination to acquire both the amplitude and phase of an object. In the proposed method, an object is illustrated by a series of coherent structured light fields which are generated by a phase-only spatial light modulator, the complex Fourier spectrum of the object can be acquired sequentially by a single-pixel photodetector. Then the desired complex-amplitude image can be retrieved directly by applying an inverse Fourier transform. We experimentally implemented this CFSI with several different types of objects. The experimental results show that the proposed method provides a promising complex-amplitude imaging approach with high quality and a stable configuration. Thus, it might find broad applications in optical metrology and biomedical science.

I. INTRODUCTION

An optical field is expressed as a complex-amplitude, which describes both the amplitude and phase of the light wave. Conventional imaging only observes amplitude information, but the important phase information is lost. This is because from the photodetector to the human retina only respond to light intensity. Developing an efficient approach to recover full complex-amplitude of an optical field has been one of the most attractive challenges in modern imaging science. Starting with early Zernike's phase contrast microscopy [1], various complex-amplitude imaging techniques have been proposed, such as differential interference contrast microscopy [2], Shack-Hartmann sensing [3], coherent diffraction imaging [4], digital holography [5], Fourier ptychographic microscopy [6], lensless ghost imaging [7–9], and phase imaging techniques based on transport-of-intensity equation [10].

However, almost all the above methods require pixelated imaging sensors. This leads to a strong challenge for the cases with a light of invisible wavelength or extremely low intensity. Because it can be impractical or prohibitively costly to implement with a pixelated imaging device. Single-pixel imaging (SPI), as an emerging imaging technique characterized by using structured illumination and a single-pixel detector, has the potential to overcome the challenge [11]. Thus, several attempts were made to achieve the complex amplitude information of objects by using SPI techniques, such as single-pixel diffractive imaging [12–14], single-pixel wavefront sensing [15–17], single-pixel ptychography [18], single-pixel digital holography [19–24], and single-pixel phase imaging based on common-path interferometry [25–30].

Benefiting from the advantages of single-pixel detectors, the complex-amplitude single-pixel imaging is becoming a promising imaging modality in the fields of optical microscopy [25], optical metrology [29], and biomedical science [24].

In this letter, we present a novel complex-amplitude Fourier single-pixel imaging (CFSI) method by combining coherent structured illumination [14, 20, 25, 27, 29] and common-path interference [25–30] with Fourier basis scan [31–34]. Different from previous CFSI methods [22, 27, 28] that use the digital micromirror device based on the super-pixel method for complex-amplitude modulation, we employ a phase-only spatial light modulator to generate both the structured light and the reference light to form the coherent structured illumination. The phase modulation proposal is relatively simple and efficient. Compared to a two-beam interferometer, the single-beam structure is more compact and stable in practical application. With the help of a 4-step phase-shifting, the complex-valued Fourier spectrum can be directly acquired by single-pixel detection. The desired complex-amplitude image can be further retrieved by applying an inverse Fourier transform. In the experiments, the proposed CFSI is implemented with three different types of objects. Experimental results demonstrate that the coherent structured illumination enable the CFSI method to have high quality and a stable configuration. In addition, we find that the undersampling technique can effectively remove noise and considerably accelerate the image acquisition process in our CFSI scheme.

II. METHODS

A. Schematic of our CFSI

The schematic of our CFSI is depicted in Fig. 1. A He-Ne laser of wavelength 632.8 nm is first expanded and collimated by a spatial filter (SF) and a collimating lens (L_1), then passes through a beam splitter (BS), and finally incident on a phase-only liquid-crystal-on-silicon spatial

* shzhang@hbu.edu.cn

† hcli@um.edu.mo

‡ liangbaolai@gmail.com

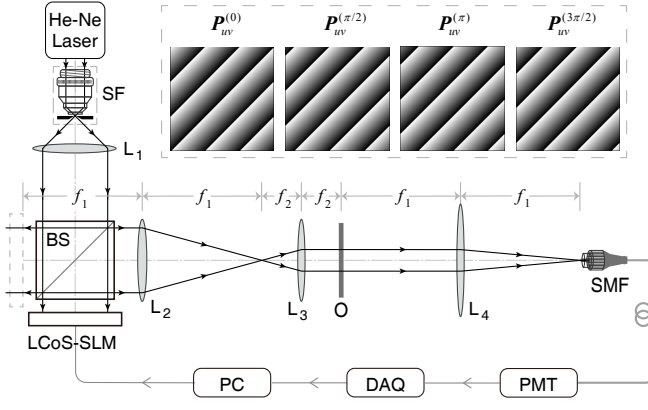


FIG. 1. Schematic of our CFSI. SF, spatial filter system; L_1 , collimating lens; BS, 50:50 non-polarizing beamsplitter; LCoS-SLM, liquid-crystal-on-silicon spatial light modulator; L_2 , L_3 , achromatic doublet lenses; O, target object; L_4 , collecting lens; SMF, single mode fiber optic patch cable; PMT, photomultiplier tube; DAQ, data acquisition board; PC, personal computer.

light modulator (LCoS-SLM). Since the modulation efficiency of the LCoS is not 100%, the reflected light consists of two parts, the phase-modulated structured light and the directly reflected light that serves as the reference light. The structured light and the reference light travel along the same path, resulting in common-path interference to form coherent structured illumination. The coherent structured illumination is reflected by BS and imaged onto the target object (O) via a $4f$ system, which consists of two achromatic doublet lenses (L_2 , L_3) with an aperture of 50 mm and focal lengths of 30 cm and 10 cm, respectively. The transmitted object light passes through a collecting lens (L_4) of focal length 30 cm and aperture 75 mm, and then reaches the single mode fiber optic patch cable (SMF). Since O and the end face of SMF are located at the front and rear focal planes of L_4 , the Fourier spectrum of the transmitted object light is obtained at the end face of SMF. Due to the core diameter of about 9 μm , SMF collects only the zero-frequency light. A photomultiplier tube (PMT) detects the light from SMF, and the resulting output is fed to PC via a data acquisition board (DAQ).

B. Fourier basis scan for the CFSI

Let the spatial sampling matrix of the complex transmittance of the target object be \mathbf{f} . By definition, the two-dimensional discrete Fourier transform can be written as

$$F(u, v) = \sum_{x=0}^{M-1} \sum_{y=0}^{N-1} f(x, y) \exp \left[-j2\pi \left(\frac{ux}{M} + \frac{vy}{N} \right) \right], \quad (1)$$

where $f(x, y)$ represents the element of the sampling matrix \mathbf{f} , $F(u, v)$ represents the Fourier spectrum component, and $u = 0, 1, \dots, M-1$, $v = 0, 1, \dots, N-1$, and M , N denote the number of rows and columns of the

sampling matrix \mathbf{f} , respectively. The complete set of Fourier basis matrices can be expressed as

$$\left\{ \mathbf{T}_{uv} \left| \begin{array}{l} u = 0, 1, \dots, \lceil M/2 \rceil - 1, -\lceil M/2 \rceil, \dots, -1, \\ v = 0, 1, \dots, \lceil N/2 \rceil - 1, -\lceil N/2 \rceil, \dots, -1. \end{array} \right. \right\}, \quad (2)$$

where the Fourier basis matrix \mathbf{T}_{uv} is defined as

$$T_{uv}(x, y) = \exp \left[-j2\pi \left(\frac{ux}{M} + \frac{vy}{N} \right) \right], \quad (3)$$

where

$$\begin{aligned} x &= -\lceil M/2 \rceil, \dots, -1, 0, 1, \dots, \lceil M/2 \rceil - 1, \\ y &= -\lceil N/2 \rceil, \dots, -1, 0, 1, \dots, \lceil N/2 \rceil - 1, \end{aligned}$$

where $\lfloor \cdot \rfloor$ and $\lceil \cdot \rceil$ denote floor and ceiling operations, respectively. Taking into account the periodicity of the discrete Fourier transform, the range of values of the spatial coordinates is shifted so that the origin of the coordinates lies at the center of the matrix, and the range of values of the spatial frequency coordinates is also shifted to facilitate the inverse discrete Fourier transform (IDFT) to reconstruct the complex transmittance of the target object. Then the Fourier spectrum coefficient $F(u, v)$ can be obtained by

$$F(u, v) = \langle \mathbf{f}, \mathbf{T}_{uv}^* \rangle_F, \quad (4)$$

where $\langle \cdot, \cdot \rangle_F$ denotes the Frobenius inner product, and $*$ denotes complex conjugate. Each Fourier spectrum coefficient can be acquired one by one, hence this technique is called Fourier basis scan.

From the definition of Eq. (3), it can be seen that the Fourier basis matrix \mathbf{T}_{uv} is a phase-only matrix with the phase distribution of $\arg \mathbf{T}_{uv} \in [0, 2\pi)$. Using the phase distribution, we can generate a phase pattern

$$\mathbf{P}_{uv} = \frac{1}{2\pi} \arg \mathbf{T}_{uv}. \quad (5)$$

We load the LCoS with the phase pattern \mathbf{P}_{uv} to generate the corresponding structured light, which has the form of $E_0 \mathbf{T}_{uv}$, where E_0 is the amplitude of the structured light. The reference light can be expressed as $E_r e^{-j\phi_r}$, where E_r is the amplitude and ϕ_r is the initial phase. Thus, the coherent structured illumination has the form of

$$\mathbf{E}_{uv} = E_0 \mathbf{T}_{uv} + E_r e^{-j\phi_r} \mathbf{1}, \quad (6)$$

where $\mathbf{1}$ denotes a matrix of ones which has the same dimension as \mathbf{T}_{uv} . Under this coherent structured illumination, the zero-frequency component of the object light measured by PMT can be expressed as

$$D(u, v) = \eta |\langle \mathbf{f}, \mathbf{E}_{uv}^* \rangle_F|, \quad (7)$$

where η represents the quantum efficiency of PMT.

A 4-step phase shift method is used to acquire the Fourier spectrum. This requests shifting the Fourier basis matrix \mathbf{T}_{uv} by $\varphi = 0, \pi/2, \pi, 3\pi/2$ to obtain a set

of phase-shifted basis matrices $\mathbf{T}_{uv}^{(\varphi)} = e^{j\varphi}\mathbf{T}_{uv}$. The corresponding phase patterns are generated by $\mathbf{P}_{uv}^{(\varphi)} = \arg\mathbf{T}_{uv}^{(\varphi)}/2\pi$, as shown in the inset of Fig. 1. We load the whole set of the phase patterns $\{\mathbf{P}_{uv}^{(\varphi)}\}$ onto the LCoS one by one and acquire the corresponding responses of PMT, denoted as $\{\mathbf{D}^{(\varphi)}(u, v)\}$. Then we can retrieve the Fourier spectrum matrix of the target object from the responses of PMT as

$$\mathbf{F} = \alpha \left\{ [\mathbf{D}^{(0)} - \mathbf{D}^{(\pi)}] + j[\mathbf{D}^{(3\pi/2)} - \mathbf{D}^{(\pi/2)}] \right\}, \quad (8)$$

where α is a complex constant. By using the IDFT, we can reconstruct the complex transmittance of the target object

$$\mathbf{f} = \text{fftshift}\{\text{ifft2}\{\mathbf{F}\}\}, \quad (9)$$

where $\text{ifft2}\{\cdot\}$ denotes the two-dimensional IDFT operation using a fast algorithm and the subsequent $\text{fftshift}\{\cdot\}$ operation shifts the coordinate origin to the center of the matrix.

III. RESULTS

In all experiments, we set the imaging resolution to 128×128 pixels, and display each pixel of the phase patterns as 2×2 LCoS pixels. Since the effective aperture is large enough, all the coherent structured illumination patterns can be imaged onto the object by the $4f$ system. As the pixel pitch of the LCoS is $8 \mu\text{m}$ and the magnification of the $4f$ system is $1/3$, the spatial resolution and the field of view of this CFSI are theoretically $5.33 \mu\text{m}$ and $682.67 \mu\text{m}$ in the experiments.

As a demonstration, we first apply our CFSI to image a glass plate etched with three intersecting discs. As shown in Fig. 2(a), the discs are all $400 \mu\text{m}$ in diameter, and the circumference of each disc passes through the centers of the other two discs. The etching depths in red, green and blue regions are 372 nm , 715 nm , and 1051 nm , respectively. This is a simple phase object. Fig. 2(b) shows the macro photo of this etched object captured by a digital camera. Fig. 2(c) shows the theoretical phase distribution of this etched object for the light of wavelength 632.8 nm , and the phase profile along the highlighted line is shown in Fig. 2(d).

Fig. 2(e) shows the magnitude of the measured spectrum. The values of the measured spectrums are linearly scaled to $[0, 1]$, but the dynamic range of the spectrum is compressed to show the high frequency components more clearly. The reconstructed amplitude and phase images are shown in Figs. 2(f) and (g), respectively, and the phase profile along the highlighted line is shown in Fig. 2(h). The values of the reconstructed amplitude images are linearly scaled to $[0, 1]$ for display. Due to the phase modulation error of LCoS-SLM, external vibration and other factors, the measured spectrum contains noises, which affect the reconstructed image quality. The low frequency noises cause a bright dot in the center of the reconstructed amplitude image, as shown in Fig.

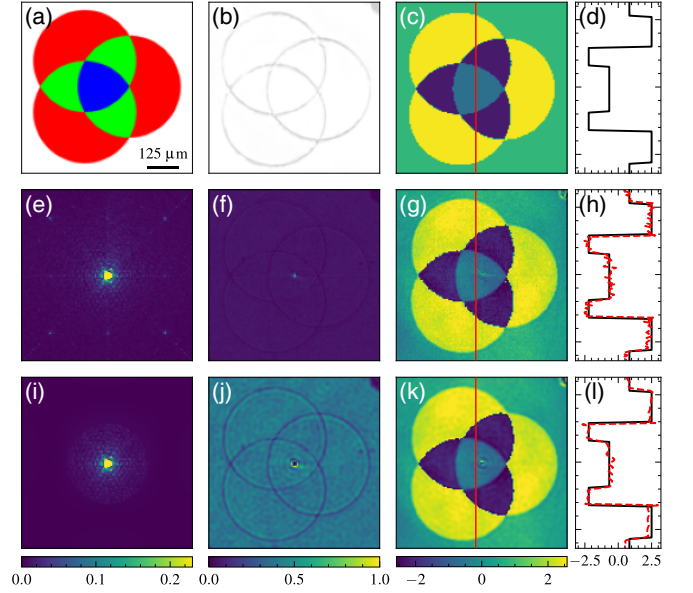


FIG. 2. The glass plate etched with three intersecting discs and related experimental results. (a) Geometry diagram of the etched discs. (b) The macro photo of the etched object. (c) The theoretical phase distribution of the etched object. (d) The phase profile along the highlighted line shown in (c). (e)–(h) are the magnitude of the measured spectrum, the reconstructed amplitude and phase images, and the phase profile at full sampling ratio, respectively, and (i)–(l) are the corresponding results at the sampling ratio of 17.2%, respectively. See Data File 1 for underlying values.

2(f). The high frequency noises, which can be seen as symmetric pairs of bright dots in the magnitude spectrum shown in Fig. 2(e), cause the reconstructed phase fluctuation, as shown in Fig. 2(h). At full sampling ratio, the imaging acquisition time is 195 minutes, which is mainly limited by the response time and phase flicker of LCoS-SLM.

The high frequency noises can be avoided by under-sampling. Here we set the sampling ratio of 17.2%, at which point the high frequency noises basically disappears, as shown in Fig. 2(i). In addition, undersampling can significantly reduce the acquisition time. At the current sampling ratio, the imaging acquisition time is about 34 minutes. To eliminate the influence of low frequency noises, we need perform noise suppression during image reconstruction, similar to that proposed by Xiao *et al.* in reference[35]. We use the subimage within the 3×3 neighborhood of the center of the reconstructed image as an estimate of the spectrum of the low frequency noises in all experiments. The final reconstructed amplitude and phase images are shown in Figs. 2(j) and (k), respectively, and the phase profile along the highlighted line is shown in Fig. 2(l). It can be seen that the reconstructed image after noise reduction has clear amplitude and smooth and accurate phase.

In the second experiment, we challenge our CFSI with a detailed phase object, which is a glass plate etched with

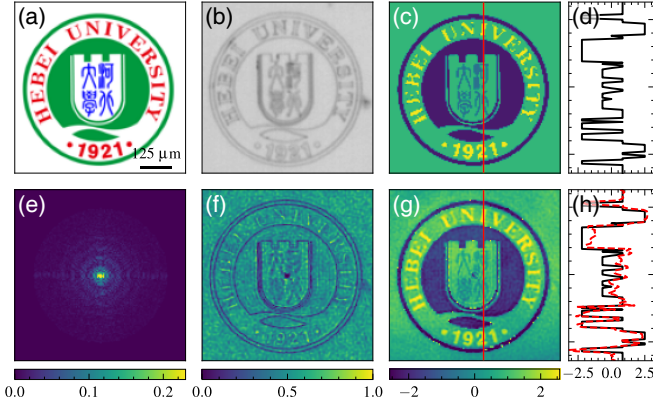


FIG. 3. The glass plate etched with the logo of Hebei University and related experimental results. (a) Geometry diagram of the etched logo. (b) The macro photo of the etched object. (c) The theoretical phase distribution of the etched object. (d) The phase profile along the highlighted line shown in (c). (e)–(h) are the magnitude of the measured spectrum, the reconstructed amplitude and phase images, and the phase profile at the sampling ratio of 47.9%, respectively. See Data File 2 for underlying values.

the logo of Hebei University. As shown in Fig. 3(a), the diameter of the logo is $600\ \mu\text{m}$, and the etching depths in the red, green and blue regions are $372\ \text{nm}$, $715\ \text{nm}$, and $1051\ \text{nm}$, respectively. Fig. 3(b) shows the macro photo of this etched object captured by a digital camera. Fig. 3(c) shows the theoretical phase distribution of this etched object for the light of wavelength $632.8\ \text{nm}$, and the phase profile along the highlighted line is shown in Fig. 3(d).

In this case, to preserve as much details as possible, we set the sampling ratio to 47.9%. The imaging acquisition time is about 257 minutes. Fig. 3(e) shows the magnitude of the measured spectrum. The reconstructed amplitude and phase images are shown in Figs. 3(f) and (g), respectively, and the phase profile along the highlighted line is shown in Fig. 3(h). It can be seen that the reconstructed amplitude image shown in Fig. 3(f) matches very well with the macro photo given in Fig. 3(b). As seen in Figs. 3(g) and 3(h) the reconstructed phase image using this CFSI are clear and accurate. However, there is a loss of some details in the reconstructed images, for example, the Chinese characters in the central region of the logo. This is due to insufficient spatial resolution in the experiment.

In the third experiment, we use a damselfly wing as the target object, to test the imaging capability of this CFSI method for natural biological tissues. We use this CFSI method to image the wing in the red box region, as shown in Fig. 4(a), and the reconstructed amplitude and phase images are shown in Figs. 4(b) and 4(c), respectively. The corresponding three-dimensional surface of the phase image is shown in Fig. 4(d). With the phase distribution, we can obtain more information about the wing. Due to less details, here we set the sampling ratio to 17.2%. In

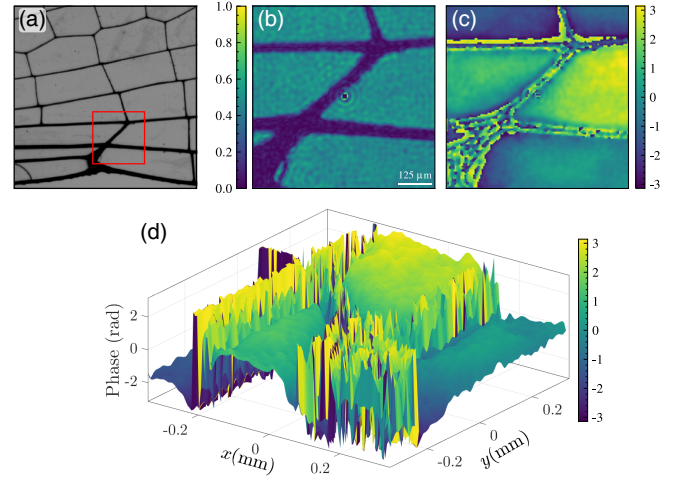


FIG. 4. The damselfly wing and related experimental results. (a) A photo of the wing. The red box indicates the imaging region. (b) and (c) are the reconstructed amplitude and phase images, respectively, at the sampling ratio of 17.2%. (d) The corresponding three-dimensional surface of the phase image (c). See Data File 3 for underlying values.

this case, the image acquisition time is about 34 minutes.

Due to vibration, lens aberrations, etc. the achievable spatial resolution is larger than the theoretical value of $5.33\ \mu\text{m}$ in practice. In the fourth experiment, we use the negative USAF-1951 resolution test chart as the target object to quantify the achievable spatial resolution in the experiments. The experimental results are shown in Fig. 5, where (a) and (b) show the amplitude image and phase image, respectively. The amplitude profiles along the highlighted lines across the horizontal and vertical

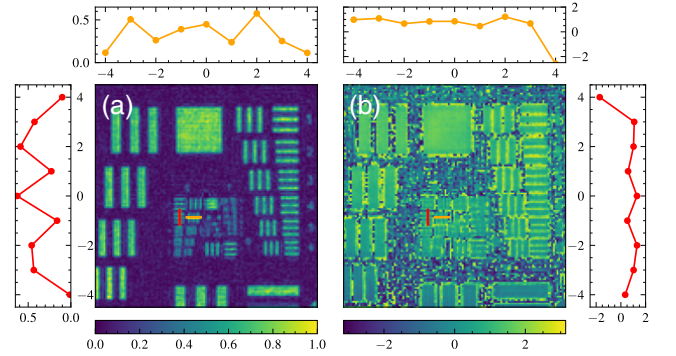


FIG. 5. Experimental results of the USAF-1951 resolution test chart. (a) and (b) are the reconstructed amplitude and phase images, respectively at the sampling ratio of 62.2%. The 4 subplots show the amplitude and phase profiles along the highlighted lines across the horizontal and vertical bars of group 6 element 3, respectively. See Data File 4 for underlying values.

bars of group 6 element 3 are shown in the left and top subplots, respectively, where the axes along the image

represent the pixel positions and each dot represents the amplitude value of one pixel. The corresponding phase profiles are also given in Fig. 5(b). As shown in Fig. 5(a), group 6 element 3 can be clearly resolved. This means that the achievable spatial resolution is about 6.2 μm . However, since the resolution test chart is a amplitude-only object, the reconstructed phase in the opaque region is severely contaminated by noise. Therefore, the spatial resolution of the phase image does not look good enough. In this case, we set the sampling ratio to 62.2%. The imaging acquisition time is about 334 minutes.

IV. CONCLUSION

In summary, we propose and experimentally demonstrate a novel complex-amplitude imaging method. By utilizing a phase-only SLM to generate coherent Fourier basis patterns as illumination, we can use a single-pixel detector to acquire the complex-valued Fourier spectrum of an object. In combination with undersampling technique and noise suppression, we can recover a high quality complex-amplitude image of the object. In experiments, we implement this CFSI method with two etched glass objects, a damselfly wing, and a resolution test chart. The reconstructed complex-amplitude images have clear amplitude, accurate phase and spatial resolution of up

to 6.2 μm . In addition, due to the use of common-path interference, the experimental configuration of this CFSI is compact and stable, which is readily integrated into commercial microscopes for quantitative phase microscopy. Thus, this complex-amplitude imaging method might find broad applications in optical metrology and biomedical science, especially for the cases with a light of invisible wavelength or extremely low intensity.

Acknowledgments

The authors are grateful to Huan Zhou for her helpful discussions and suggestions. This work was supported by the Natural Science Foundation of Hebei province (F2019201446), the Multi-Year Research Grant of University of Macau (MYRG2020-00082-IAPME), the Science and Technology Development Fund from Macau SAR (FDCT) (0062/2020/AMJ), the Advanced Talents Incubation Program of the Hebei University (8012605), and the National Natural Science Foundation of China (NSFC) (11204062, 61774053, 11674273).

DATA AVAILABILITY

Data underlying the results presented in this paper are available in Dataset (Ref. [36]).

-
- [1] F. Zernike, Phase contrast, a new method for the microscopic observation of transparent objects, *Physica* **9**, 686 (1942).
 - [2] G. Nomarski, Differential micointerferometer with polarized waves, *J. Phys. Radium Paris* **16**, 9S (1955).
 - [3] R. V. Shack, Production and use of a lecticular hartmann screen, *Journal of The Optical Society of America* **61**, 656 (1971).
 - [4] J. Miao, P. Charalambous, J. Kirz, and D. Sayre, Extending the methodology of X-ray crystallography to allow imaging of micrometre-sized non-crystalline specimens, *Nature* **400**, 342 (1999).
 - [5] P. Marquet, B. Rappaz, P. J. Magistretti, E. Cuche, Y. Emery, T. Colomb, and C. Depeursinge, Digital holographic microscopy: A noninvasive contrast imaging technique allowing quantitative visualization of living cells with subwavelength axial accuracy, *Optics Letters* **30**, 468 (2005).
 - [6] G. Zheng, R. Horstmeyer, and C. Yang, Wide-field, high-resolution Fourier ptychographic microscopy, *Nature Photonics* **7**, 739 (2013).
 - [7] D.-J. Zhang, Q. Tang, T.-F. Wu, H.-C. Qiu, D.-Q. Xu, H.-G. Li, H.-B. Wang, J. Xiong, and K. Wang, Lensless ghost imaging of a phase object with pseudo-thermal light, *Applied Physics Letters* **104**, 121113 (2014).
 - [8] H. Yu, R. Lu, S. Han, H. Xie, G. Du, T. Xiao, and D. Zhu, Fourier-Transform Ghost Imaging with Hard X Rays, *Physical Review Letters* **117**, 113901 (2016).
 - [9] Y.-N. Zhao, S.-H. Zhang, W.-L. Cui, D.-Z. Cao, and B.-L. Liang, Correlated reconstruction for the phase-only Fourier hologram with incoherent illumination, *Journal of Optics* **23**, 055603 (2021).
 - [10] C. Zuo, J. Li, J. Sun, Y. Fan, J. Zhang, L. Lu, R. Zhang, B. Wang, L. Huang, and Q. Chen, Transport of intensity equation: A tutorial, *Optics and Lasers in Engineering* **135**, 106187 (2020).
 - [11] G. M. Gibson, S. D. Johnson, and M. J. Padgett, Single-pixel imaging 12 years on: A review, *Optics Express* **28**, 28190 (2020).
 - [12] K. Lee and J. Ahn, Single-pixel coherent diffraction imaging, *Applied Physics Letters* **97**, 241101 (2010).
 - [13] R. Horisaki, H. Matsui, R. Egami, and J. Tanida, Single-pixel compressive diffractive imaging, *Applied Optics* **56**, 1353 (2017).
 - [14] R. Horisaki, H. Matsui, and J. Tanida, Single-pixel compressive diffractive imaging with structured illumination, *Applied Optics* **56**, 4085 (2017).
 - [15] G. A. Howland, D. J. Lum, and J. C. Howell, Compressive wavefront sensing with weak values, *Optics Express* **22**, 18870 (2014).
 - [16] S. Shin, K. Lee, Y. Baek, and Y. Park, Reference-Free Single-Point Holographic Imaging and Realization of an Optical Bidirectional Transducer, *Physical Review Applied* **9**, 044042 (2018).
 - [17] F. Soldevila, V. Durán, P. Clemente, J. Lancis, and E. Tajahuerce, Phase imaging by spatial wavefront sampling, *Optica* **5**, 164 (2018).
 - [18] M. Li, L. Bian, G. Zheng, A. Maiden, Y. Liu, Y. Li, J. Suo, Q. Dai, and J. Zhang, Single-pixel ptychography, *Optics Letters* **46**, 1624 (2021).
 - [19] P. Clemente, V. Durán, E. Tajahuerce, P. Andrés, V. Climent, and J. Lancis, Compressive holography with a single-pixel detector, *Optics Letters* **38**, 2524 (2013).

- [20] L. Martínez-León, P. Clemente, Y. Mori, V. Climent, J. Lancis, and E. Tajahuerce, Single-pixel digital holography with phase-encoded illumination, *Optics Express* **25**, 4975 (2017).
- [21] H. González, L. Martínez-León, F. Soldevila, M. Araiza-Esquivel, J. Lancis, and E. Tajahuerce, High sampling rate single-pixel digital holography system employing a DMD and phase-encoded patterns, *Optics Express* **26**, 20342 (2018).
- [22] X. Hu, H. Zhang, Q. Zhao, P. Yu, Y. Li, and L. Gong, Single-pixel phase imaging by Fourier spectrum sampling, *Applied Physics Letters* **114**, 051102 (2019).
- [23] A. Santos-Amador, M. Araiza-Esquivel, H. González, A. Rodríguez-Cobos, E. Tajahuerce, L. Martínez-León, G. Ramírez-Flores, and R. E. Balderas-Navarro, Phase and amplitude reconstruction in single-pixel transmission microscopy: A comparison of Hadamard, cosine, and noiselet bases, *Applied Optics* **60**, 6935 (2021).
- [24] D. Wu, J. Luo, G. Huang, Y. Feng, X. Feng, R. Zhang, Y. Shen, and Z. Li, Imaging biological tissue with high-throughput single-pixel compressive holography, *Nature Communications* **12**, 4712 (2021).
- [25] Y. Liu, J. Suo, Y. Zhang, and Q. Dai, Single-pixel phase and fluorescence microscope, *Optics Express* **26**, 32451 (2018).
- [26] R. Liu, S. Zhao, P. Zhang, H. Gao, and F. Li, Complex wavefront reconstruction with single-pixel detector, *Applied Physics Letters* **114**, 161901 (2019).
- [27] S. Zhao, R. Liu, P. Zhang, H. Gao, and F. Li, Fourier single-pixel reconstruction of a complex amplitude optical field, *Optics Letters* **44**, 3278 (2019).
- [28] Y. Liu, P. Yu, X. Hu, Z. Wang, Y. Li, and L. Gong, Single-pixel spiral phase contrast imaging, *Optics Letters* **45**, 4028 (2020).
- [29] X. Li, Y. Sun, Y. He, X. Li, and B. Sun, Quantitative imaging for optical field via a single-pixel detector, *Signal Processing* **188**, 108173 (2021).
- [30] H.-Y. Hou, Y.-N. Zhao, J.-C. Han, S.-W. Cui, D.-Z. Cao, H.-C. Liu, S.-H. Zhang, and B.-L. Liang, Complex-amplitude single-pixel imaging using coherent structured illumination, *Optics Express* **29**, 41827 (2021).
- [31] Z. Zhang, X. Ma, and J. Zhong, Single-pixel imaging by means of Fourier spectrum acquisition, *Nature Communications* **6**, 6225 (2015).
- [32] J. Huang, D. Shi, K. Yuan, S. Hu, and Y. Wang, Computational-weighted Fourier single-pixel imaging via binary illumination, *Optics Express* **26**, 16547 (2018).
- [33] Z. Zhang, S. Liu, J. Peng, M. Yao, G. Zheng, and J. Zhong, Simultaneous spatial, spectral, and 3D compressive imaging via efficient Fourier single-pixel measurements, *Optica* **5**, 315 (2018).
- [34] J. Peng, M. Yao, Z. Huang, and J. Zhong, Fourier microscopy based on single-pixel imaging for multi-mode dynamic observations of samples, *APL Photonics* **6**, 046102 (2021).
- [35] Y. Xiao, L. Zhou, and W. Chen, Direct Single-Step Measurement of Hadamard Spectrum Using Single-Pixel Optical Detection, *IEEE Photonics Technology Letters* **31**, 845 (2019).
- [36] Y.-N. Zhao, H.-Y. Hou, J.-C. Han, D.-Z. Cao, S.-H. Zhang, H.-C. Liu, and B.-L. Liang, Complex-amplitude fourier single-pixel imaging via coherent structured illumination-dataset, figshare. Dataset. 10.6084/m9.figshare.18070493.v2 (2022).